

Disorder-resilient transition of Helical to Conical ground states in $M_{1/3}NbS_2$, $M=Cr, Mn$

M. Sahoo,^{1,2,3} P. Bonfà,¹ A. E. Hall,⁴ D. A. Mayoh,⁴ L. T. Corredor,² A. U.
B. Wolter,² B. Büchner,^{2,3} G. Balakrishnan,⁴ R. De Renzi,^{1,*} and G. Allodi¹

¹*Dipartimento di Scienze Matematiche, Fisiche ed Informatiche,
Università di Parma, Parco Area delle Scienze 7A, I-43100 Parma, Italy*

²*Leibniz IFW Dresden, Helmholtzstraße 20, D-01069 Dresden, Germany*

³*Institut für Festkörper- und Materialphysik and Würzburg-Dresden Cluster of Excellence ct.qmat,
Technische Universität Dresden, 01062 Dresden, Germany*

⁴*Department of Physics, University of Warwick, Coventry, CV4 7AL, United Kingdom*

(Dated: October 3, 2024)

The discovery of chiral helical magnetism (CHM) in $Cr_{1/3}NbS_2$ and the stabilization of a chiral soliton lattice (CSL) has attracted considerable interest in view of their potential technological applications. However, there is an ongoing debate regarding whether the sister compound, $Mn_{1/3}NbS_2$, which shares the same crystal structure, exhibits similar nontrivial properties which rely on the stabilization of the lack of inversion symmetry at the magnetic ion. In this study, we conduct a comprehensive investigation of the magnetically ordered states of both compounds, using ^{53}Cr , ^{55}Mn and ^{93}Nb nuclear magnetic resonance. Our results, supported by density functional calculations, detect in a high-quality single crystal of $Cr_{1/3}NbS_2$ all the signatures of the monoaxial CHM in a magnetic field, identifying it as a textbook NMR case. The detailed understanding of this prototypic behavior provides a reference for $Mn_{1/3}NbS_2$. Despite the much larger density of specific defects in this second single crystal, we confirm the presence of a CHM phase in the Mn compound, characterized by a very large critical field for the forced ferromagnetic phase (≈ 5 T for the applied field along c).

I. INTRODUCTION

Layered transition metal dichalcogenides (TMDCs), denoted as XY_2 , where X represents a transition metal (e.g., Nb, Ta) and Y represents a chalcogen (e.g., S, Se), have garnered significant attention owing to their intriguing electrical and optical properties [1–5]. Despite being nonmagnetic, the weak van der Waals bonding between the layers in XY_2 allows for remarkable tunability within 2D limits and it also enables the intercalation of magnetic 3d transition metals, leading to the formation of ternary TMDC-based magnetic compounds ($M_{1/3}XY_2$, where M can be Cr, Mn, V, Fe, Co, Ni) exhibiting diverse structural and magnetic properties [6, 7], including strong spin-orbit coupling. Sulfur-based compounds, in particular, feature localized moments arising from the spins of unpaired electrons at the intercalant sites because the orbital moment is often quenched due to the crystal field effects from neighboring sulfur atoms [7, 8]. The magnetic properties are largely dictated by the type and concentration of the intercalants; for instance, Cr, and Mn-based TMDCs exhibit dominant ferromagnetic interactions, while for V, Co and Ni-based ones the dominant exchange is antiferromagnetic [6, 9]. Recent studies on $M_{1/3}NbS_2$, where M can be Cr or Mn, have unveiled the emergence of chiral helimagnetism [10–16]. This discovery opens up new avenues for exploring novel properties and potential technological applications, marking an exciting development in the field of TMDCs [17, 18].

The chiral magnetism observed in $Cr_{1/3}NbS_2$, which belongs to the non-centrosymmetric space group $P6_322$, originates from the arrangement of intercalant atoms forming a $\sqrt{3} \times \sqrt{3}$ superlattice in a bilayer triangular configuration. The broken inversion symmetry, described by the Dzyaloshinskii-Moriya (DM) interaction, competes with the in-plane ferromagnetic Heisenberg exchange interaction (J), leading to the emergence of chiral helimagnetic order (CHM) along the c -axis at zero magnetic fields. The direction of spin rotation and the chirality of the system are determined by the sign of the DM vector [12, 13, 19, 20]. The ratio between the DM vector and J gives the periodicity of the CHM phase in the sample and is extremely important; however, the chirality of these compounds may be compromised by structural disorder [21]. Under the influence of a magnetic field, CHM transforms into various nonlinear magnetic structures. For instance, applying the field along the chiral axis ($\mathbf{H} \parallel \hat{c}$) results in chiral conical phases (CCP), whereas applying the field within the ab plane ($\mathbf{H} \perp \hat{c}$) leads to the formation of a chiral soliton lattice (CSL) phase. Both phases arise due to different magnetic energies competing with the incommensurate CHM phase. Further increasing the magnetic field transforms the incommensurate phase into a commensurate forced ferromagnetic (FFM) phase above a certain critical magnetic field, aligning all the spins along the field direction [12, 13, 19, 20, 22–24].

While the magnetic phase transitions in the $Cr_{1/3}NbS_2$ sample are well established, the isostructural compound $Mn_{1/3}NbS_2$ remains a topic of discussion. It has been suggested to exhibit a similar chiral helimag-

* Corresponding address: roberto.derenzi@unipr.it

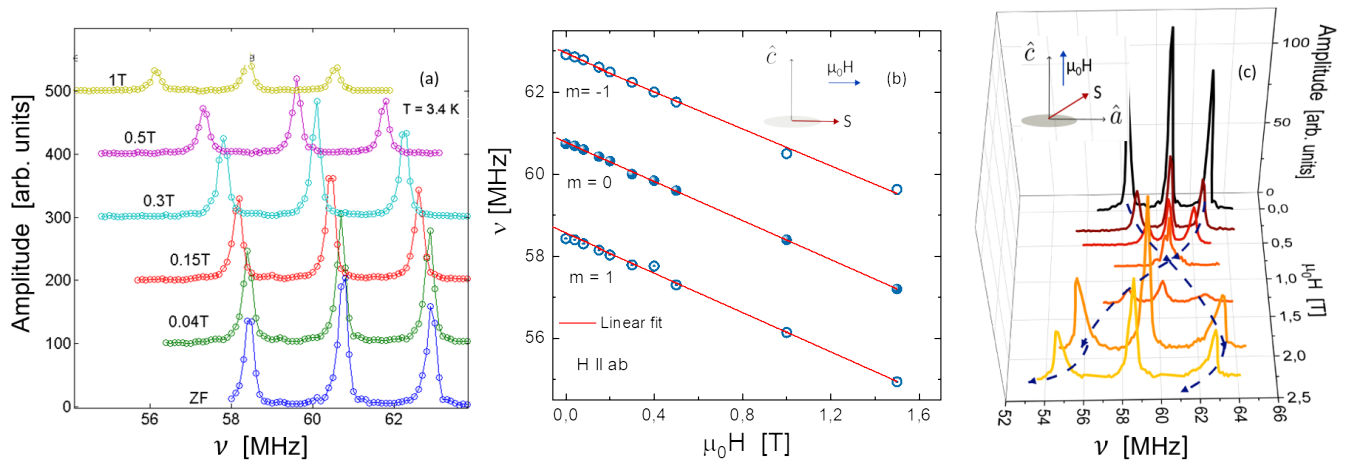


FIG. 1. Representative ^{53}Cr NMR spectra at $T = 3.4$ K for (a) $\mathbf{H} \perp c$, displaced vertically for clarity, with best fit; (b) the corresponding best fit peak frequencies vs. H with their three linear regressions (red solid lines), and (c) representative spectra for $\mathbf{H} \parallel c$ at $T = 3.4$ K, with best fit.

netic (CHM) and topological soliton lattice. [10, 15, 25] However, recent reports on this compound have not been able to distinguish between trivial ferromagnetic domains with π domain walls and non-trivial ferromagnetic regions periodically divided by chiral soliton kinks of spins (2π domain walls) [24, 25]. The observation of a large pitch length in the helimagnetic phase and the presence of short-range ferromagnetic domains of ≈ 250 nm, as noted by Karna et al. [15], despite not excluding the CSL, complicate the identification.

In addition to magnetometry and more direct identification offered by neutron scattering and electron microscopy, various spin structures and magnetic phases can be explored using local microscopic techniques such as muon spin relaxation (μSR) and nuclear magnetic resonance (NMR). In particular μSR has helped to identify different phases by analyzing the amplitude of the magnetic fraction in both zero fields and applied fields, suggesting the presence of helimagnetic phase below 50K [13]. Similarly, zero-field NMR has been employed to try to identify the various valence states resulting from disorder in the compound [26, 27].

The present work is organized as follows. In Sec. II A we describe the common expected spectral patterns and in Sec. II B we present an extensive set of zero-field (ZF) and field-dependent ^{53}Cr NMR measurements on our $\text{Cr}_{1/3}\text{NbS}_2$ single crystals in two different field orientations, which identify the different field ranges of the CSL, CCP and FFM phases, characteristic of a monoaxial chiral helimagnet [10], setting a reference standard for the still controversial case of the $\text{Mn}_{1/3}\text{NbS}_2$ compound. Moreover, we directly observe that the phase transition in $\text{Cr}_{1/3}\text{NbS}_2$ from chiral helimagnetic (CHM) to paramagnetic is of the first order. Additional insight is obtained from ^{93}Nb NMR in Sec. II C. The ^{55}Mn NMR results from the $\text{Mn}_{1/3}\text{NbS}_2$ spectra and the assignment supported by DFT calculations are presented in Sec. II D.

The unique attribution of the spectral features is complicated by the larger occupancy of the Mn $2b$ and $2d$ Wyckoff sites, resulting in multi-modal inhomogeneous magnetic broadening. Despite this shortfall, the demonstration that $\text{Mn}_{1/3}\text{NbS}_2$ is also a chiral helical magnet is confirmed by the observation of large amplitude spin echo oscillations that reveal the same type of interplay of quadrupolar and magnetic interactions as in the $\text{Cr}_{1/3}\text{NbS}_2$ case. Discussion with conclusions and the description of the methods follow in Sec. III and Sec. IV, respectively.

II. NMR RESULTS

The ^{53}Cr , ^{55}Mn and ^{93}Nb nuclei, all with spin $I > \frac{1}{2}$, obey the same spin Hamiltonian in $\text{Cr}_{1/3}\text{NbS}_2$ and $\text{Mn}_{1/3}\text{NbS}_2$ consisting in a hierarchy of hyperfine, quadrupolar and Zeeman couplings, albeit with different parameter values. From the NMR results, we demonstrate that the magnetic properties of the two compounds are similar, but the results themselves are largely distinguished by different relative scales of the three interactions and different sample characteristics. We briefly introduce here the nuclear spin interactions, while more details are provided in Sec. IV

A. Commonalities of the NMR spectra.

The properties of the ^{53}Cr , ^{55}Mn and ^{93}Nb nuclear isotopes are summarized in Tab. I The single-crystal low-temperature NMR spectrum from each of them is qualitatively understood considering that the cylindrical, nearly isotropic hyperfine field tensor \mathbf{B}_{hf} dominates on the smaller quadrupole coupling ($\nu_Q \ll \nu_{\text{hf}} = \gamma B_{\text{hf}}$). This produces a pattern of $2I$ frequencies, in first ap-

TABLE I. Nuclear spin, gyromagnetic ratios, quadrupole moments and natural abundance of ^{53}Cr , ^{55}Mn , ^{93}Nb

Isotope	I	γ [MHz/T]	Q [fm ²]	Natural abundance
^{53}Cr	$\frac{3}{2}$	2.4115	-15(5) [28] -8.4 [29]	0.095
^{55}Mn	$\frac{5}{2}$	10.5763	33(1)	1.0
^{93}Nb	$\frac{9}{2}$	10.4523	32(2)	1.0

proximation equally spaced and centered at the Larmor frequency corresponding to the internal field at the nucleus. Since the hyperfine tensor and electric field gradient (EFG) tensor that couples to the nuclear electric quadrupole moment share the same principal axis, $\hat{z} = \hat{c}$, the two simple experimental conditions are with \mathbf{H} either parallel or perpendicular to \hat{c} . In the first case, the angle $\theta = \theta(H)$ between the electron spin \mathbf{S} and the easy-plane ($\perp \hat{c}$) determines both the direction of the hyperfine field \mathbf{B}_{hf} and the quadrupolar splitting, producing the following frequency pattern in first-order perturbation

$$\nu_m^\perp(H) = \gamma|B_{\text{hf}}^x - \mu_0 H| + \Delta\nu_m(0), \quad (1)$$

where $-I \leq m \leq I$ and $\mathbf{B} = \mu_0 \mathbf{H}$ is the applied magnetic field. For \mathbf{B} along the c axis

$$\nu_m^\parallel(H, \theta) = \gamma B_{\text{loc}} + \Delta\nu_m(\theta), \quad (2)$$

where

$$B_{\text{loc}} = ((B_{\text{hf}}^x \cos \theta)^2 + (B_{\text{hf}}^z \sin \theta - \mu_0 H)^2)^{\frac{1}{2}},$$

$$\Delta\nu_m(\theta) = m\nu_Q \frac{3 \sin^2 \theta - 1}{2}, \quad (3)$$

and the relative sign of H and B_{hf} is due to the electron moment being opposite to the electron spin. Equations 1-3 predict $2I = 3, 5,$ and 9 lines for Cr, Mn and Nb, respectively and the field dependence is close to the exact one, but best fits of the data are refined by numerical diagonalization of the full spin Hamiltonian 5, beyond first-order approximation.

B. ^{53}Cr NMR in $\text{Cr}_{1/3}\text{NbS}_2$.

Figure 1 (a) shows the expected triplet of NMR lines obtained in zero applied field (ZF) for the Cr single crystal, together with the shifted spectra measured with $\mathbf{H} \perp \hat{c}$ at 3.4 K. The ZF central frequency is around 61 MHz (i.e. $|B_{\text{hf}}| = 25.34$ T). Triplet spectra are fitted to a minimal set of Gaussian components. The peak position for each of the three components is defined as its center of gravity (the first moment, see Eq. 11). The rigid shift of these triplet peaks towards lower frequencies, shown in Fig. 1 (b) for this crystal orientation, with slope equal to $^{53}\gamma$, indicates that the applied and internal field add collinearly according to Eq. 1 in the forced ferromagnetic

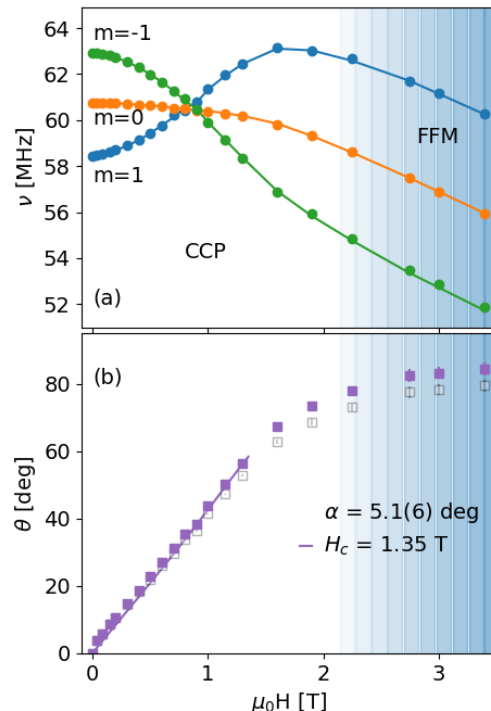


FIG. 2. (a) ^{53}Cr peak frequencies vs. field from the $\mathbf{H} \parallel \hat{c}$ spectra of Fig. 1 (c), with best fit curves (solid lines, see text). (b) Field dependence of the best fit conical angles $\theta(H)$ with (purple) and without (gray) correction for experimental misalignment ϕ between the field direction and \hat{c} (symbols), with best fit to Eq. 4.

(FFM) phase expected for this easy plane chiral magnet. [30]

The more complex pattern predicted by Eq. 2 for the other crystal orientation, $\mathbf{H} \parallel \hat{c}$ is indeed displayed in Fig. 1 (c). Notably, the triplet splitting vanishes at the angle $\theta = \sin^{-1} \frac{1}{3}$, in agreement with Eq. 3. The peak positions are shown in Fig. 2 (a) vs. field. In first order, they agree with Eq. 2, but the global best fit (dashed line) is obtained by numerical diagonalization, optimizing the common hyperfine and quadrupolar parameters reported in Tab. II, together with a separate, local angle $\theta(H)$ for the three data points at each experimental field value. The latter are displayed in Fig. 2 (b) and, taking carefully into account the small experimental misalignment, [31] they agree with mean field predictions [30, 31]

$$\theta(H) = \sin^{-1} \left(\frac{H}{H_c} \right) \quad (4)$$

(bear in mind that θ is the field angle from the plane). Here $\mu_0 H_c = 2S(\sqrt{J^2 + D^2} - J + K_\perp)/g\mu_B = 1.35(1)$ T, g is the Cr $S = 3/2$ Landé factor, J, D, K_\perp are the Heisenberg, Dzyaloshinskii-Moriya exchange and the easy axis anisotropy constants, respectively.

Let us turn now to the microscopic magnetization, measured by the hyperfine field (Sec. IV B), and largely

TABLE II. ^{53}Cr global best fit parameters for Fig. 2.

ν_Q [MHz]	B_{hf}^x [T]	B_{hf}^z [T]	ϕ [deg]
4.49(3)	25.172(3)	26.63(1)	5.1((6)

dominated by the on-site contribution. The typical value for the on-site isotropic hyperfine fields in transition metal ions is $B_{\text{hf}} = \mathcal{A}\mu$, with μ the electron magnetic moment in Bohr magnetons and an average hyperfine coupling $\mathcal{A} \approx 10 \text{ T}/\mu_B$. Therefore, the mean hyperfine field value of 26 T in Tab. II roughly corresponds to $2.6\mu_B$. According to Eqs. 1 and 3, the temperature dependence of the central transition frequency ν_0 in the ZF ^{53}Cr -NMR triplets provides $^{53}\gamma B_{\text{hf}}^x(T)$, proportional to the atomic moment $\mu(T)$ on Cr, and leads to the values plotted in Fig. 3 (a). Notice that the decrease of the NMR amplitude $A(T)$ in Fig. 3 (b), in the highlighted pre-transition region, $90 \text{ K} < T \leq T_m$, is typical of a first-order transition. It shows that paramagnetic domains start developing well below the transition temperature T_m , and average electron spin value $S(T)$ in the residual ordered domains remains large (the hyperfine field at T_m is still more than half of its zero temperature value).¹

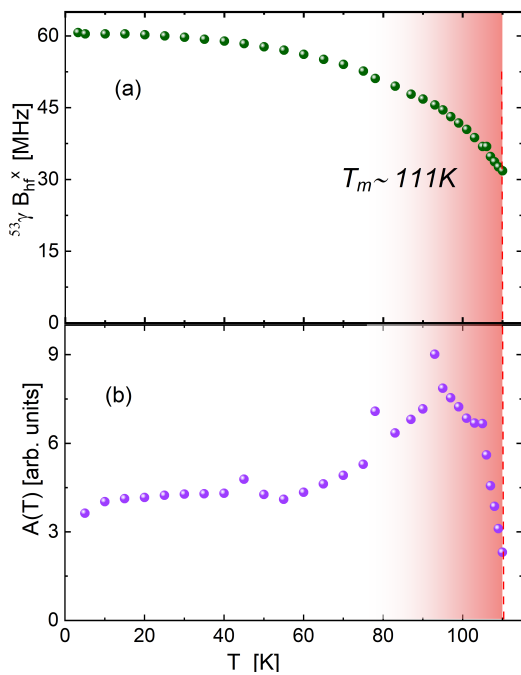


FIG. 3. Temperature dependence of: (a) the ^{53}Cr hyperfine frequency $^{53}\gamma B_{\text{hf}}^x \propto \mu(T)$; (b) its NMR amplitude $A(T)$, corrected for the nuclear Curie law.

¹Instead, the smoother increase of $A(T)$ from 60 to 90 K is due to magnetic anisotropy reduction, which provides a larger ferromagnetic enhancement – see Sec.IV; notice that the first-order loss of amplitude is clearly visible, *despite* this amplified NMR sensitivity.

TABLE III. ^{93}Nb quadrupolar and hyperfine parameter of the 2-site best fit (Eq. 8 in Fig. 4).

Wyckoff site	fraction	ν_Q [MHz]	ν_{hf} [MHz]	$\delta\nu$ [MHz]
2a	0.33	0.9	8.9	0.19
2b	0.67	1.23	13.8	0.21

C. ^{93}Nb NMR in $\text{Cr}_{1/3}\text{NbS}_2$.

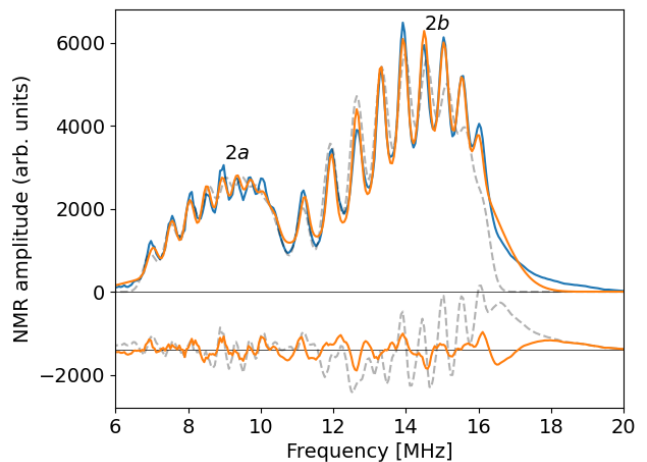


FIG. 4. Zero-field (blue curve) ^{93}Nb NMR spectrum at $T = 1.3 \text{ K}$ in $\text{Cr}_{1/3}\text{NbS}_2$ with its and 2-site (gray dashed) and 4-site (orange solid) best fits, see Sec. IV. The residues are plotted with a negative offset and the same colors.

The blue curve in Fig. 4 shows the polycrystalline ZF NMR spectrum of ^{93}Nb . By inspection we recognize two replica of the nine quadrupolar transitions predicted by Eq. 1 for nuclear spin $I = \frac{9}{2}$, that can be attributed to the two inequivalent sites Nb 2a and 2b, in the ratio 1:2 per cell. The separation of the two nonuplets is proportional to the difference of their hyperfine fields $^{93}B_{2b} - ^{93}B_{2a} \approx 0.5 \text{ T}$, roughly 0.8 and 1.3 T, respectively. These fields are too large to be due to distant dipoles on Cr ions (a very rough estimate of the dipolar field yields 0.2 T). The larger field value indicates a dominant contribution from a local moment on Nb, due to Cr-Nb hybridization.

The best fit curves in Fig. 4 require pairs of Nb sites with occupancies in the ratio 1:2, as per Wyckoff sites 2a and 2b in crystal group 181. The simplest model, with just these two main sites (Tab. III) corresponds to the gray dashed curve. A refined model with an additional pair of sites corresponding to 6% of the Nb nuclei is shown by the orange curve and it will be discussed later.

Figure 5 shows that the application of an external field to a polycrystalline sample produces two or three broad peaks, label $\alpha = 0, 2a, 2b$ denoting inequivalent Nb sites (the second two by their Wyckoff notation). All peaks shift to higher frequencies as the corresponding dashed $^{93}\gamma\mu_o H + \nu_{\text{hf}}^\alpha$ lines. The center of each peak is due to

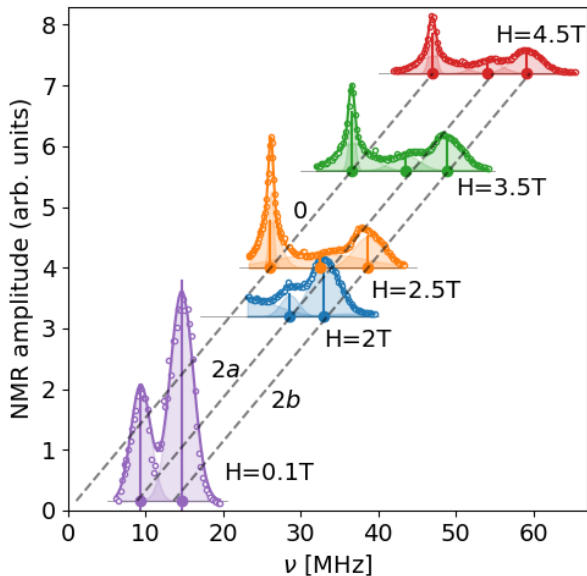


FIG. 5. ^{93}Nb NMR spectra in applied fields H at $T = 1.3$ K, shifted along the vertical axis proportionally to H . The lines correspond to $^{93}\gamma\mu_0H + \nu_{\text{hf}}$; the quadrupole splitting is hidden by the inhomogeneous magnetic broadening due to the powder average.

the more abundant crystal grains with \hat{c} orthogonal to the external field, by Eqs. 2–3 this behavior is opposite to that of ^{53}Cr and indicates that the moment on Nb is antiparallel to that of neighbor Cr ions. The NMR data also evidences the sizable presence of Nb sites ($\alpha = 0$) with a vanishing hyperfine field, discussed in Sec. III A.

D. ^{55}Mn NMR in $\text{Mn}_{1/3}\text{NbS}_2$.

Figure 6 (a) and (c) show a selection of ^{55}Mn NMR low temperature spectra obtained in a $\text{Mn}_{1/3}\text{NbS}_2$ single crystal at $T = 1.7$ K from ZF up to $H = 2$ T, with $\mathbf{H} \perp \hat{c}$ and $\parallel \hat{c}$, respectively, covering the range of 440–490 MHz. In low fields, they are centered around 470 MHz. We identify a few prominent components, consisting of overlapping peaks, which gradually change shape while shifting towards lower frequencies with the field.

We must note a few experimental differences between the ^{55}Mn case and the reference ^{53}Cr data of Fig. 1 (a) and (c), before making a comparison. First of all, the ^{55}Mn NMR amplitude at low fields is affected by very fast, field-dependent T_2^{-1} relaxation rates, which, e.g., heavily suppress the 450 MHz component in ZF.² Furthermore, the much larger gyromagnetic ratio of

^{55}Mn (roughly a factor four, see Tab. I) and the larger Mn moment per ion (roughly a factor two) modify the prediction of Eqs. 1, 2, producing eight times larger hyperfine frequencies, in agreement with the experimental ratio of about 470 MHz to 60 MHz. This implies that magnetic defects should also yield larger inhomogeneous linewidths, scaling from 0.3 MHz on ^{53}Cr to 2.4 MHz on ^{55}Mn . However, the distribution of magnetic defects in $\text{Mn}_{1/3}\text{NbS}_2$ makes the spectral peaks even broader than predicted above, with linewidths well in excess of 5 MHz, which completely hides the quadrupolar splittings in this sample.

If $\text{Mn}_{1/3}\text{NbS}_2$ were another textbook case, like $\text{Cr}_{1/3}\text{NbS}_2$, a *single broad* line would be expected, with a field dependence similar to that of the central $^{53}\nu_0$ (Fig. 1 (b), filled blue symbols, and Fig. 2 (a), orange symbols). Unfortunately, the ^{55}Mn spectra show more than one broad component, and they are separated by up to 35 MHz, a much larger and more diverse splitting than that expected for the quadrupole pattern, which is composed of five much closer, equally spaced lines for ^{55}Mn , spin $I = 5/2$. These quintuplets are convoluted by the larger magnetic inhomogeneous broadening, hence hidden within the linewidth. In conclusion, the origin of the multimodal distributions of hyperfine fields must stem from magnetically different local surroundings.

Let us concentrate on panel (a) in Fig. 6, $\mathbf{H} \perp \hat{c}$. We have already mentioned three main components: the more intense peaks at lower frequencies, originating in ZF at 455 and 475 MHz, labeled I and II, respectively, and a much weaker peak around 490 MHz, labeled III in Fig. 6 (a). Its higher frequency indicates a fractionally larger valence and a comparably larger magnetic moment. Despite the larger error bars we can compare the field dependence of their first moments in Fig. 6 (b) with those of ^{53}Cr : for $\mathbf{H} \perp \hat{c}$ (red solid symbols), peak III shifts to lower frequency with a slope in agreement with $^{55}\gamma$ (dash-dotted red line). This is expected in an easy plane ferromagnet when the spin aligns along \mathbf{H} and the magnetic moment (hence the hyperfine field) aligns opposite to \mathbf{H} . Peak III is thus identified as a small $\text{Mn}_{1/4}\text{NbS}_2$ fraction, characterized by mean valence closer to Mn^{+2} . [32]

Figure 6 (b) further shows that components I and II for $\mathbf{H} \perp \hat{c}$ (solid blue, black symbols) follow at high field a behavior similar to that of III (dash-dotted red lines), in agreement with Eq. 1, $m = 0$. Only at lower fields, where a chiral soliton phase is expected, they depart from this linear field dependence, characterized by the full gyromagnetic ratio. In contrast, for $\mathbf{H} \parallel \hat{c}$ the field slopes (open light and dark blue symbols) show a stronger deviation in the whole field range, in qualitative agreement with Eq. 2, $m = 0$ and the ^{53}Cr $m = 0$ transition of Fig. 2 (a). We attribute components I and II to the majority $\text{Mn}_{1/3}\text{NbS}_2$ structure, in two distinct, possibly defect-free and defect-related configurations, further discussed in Sec. III B.

We obtain strong support for this tentative assignment by considering the peculiar spin-echo (T_2) relaxation of

²When T_2 is comparable to the dead-time of our NMR probe, the signal becomes marginal and difficult to reliably correct for relaxation, leading to a partial, so-called, *wipeout*.

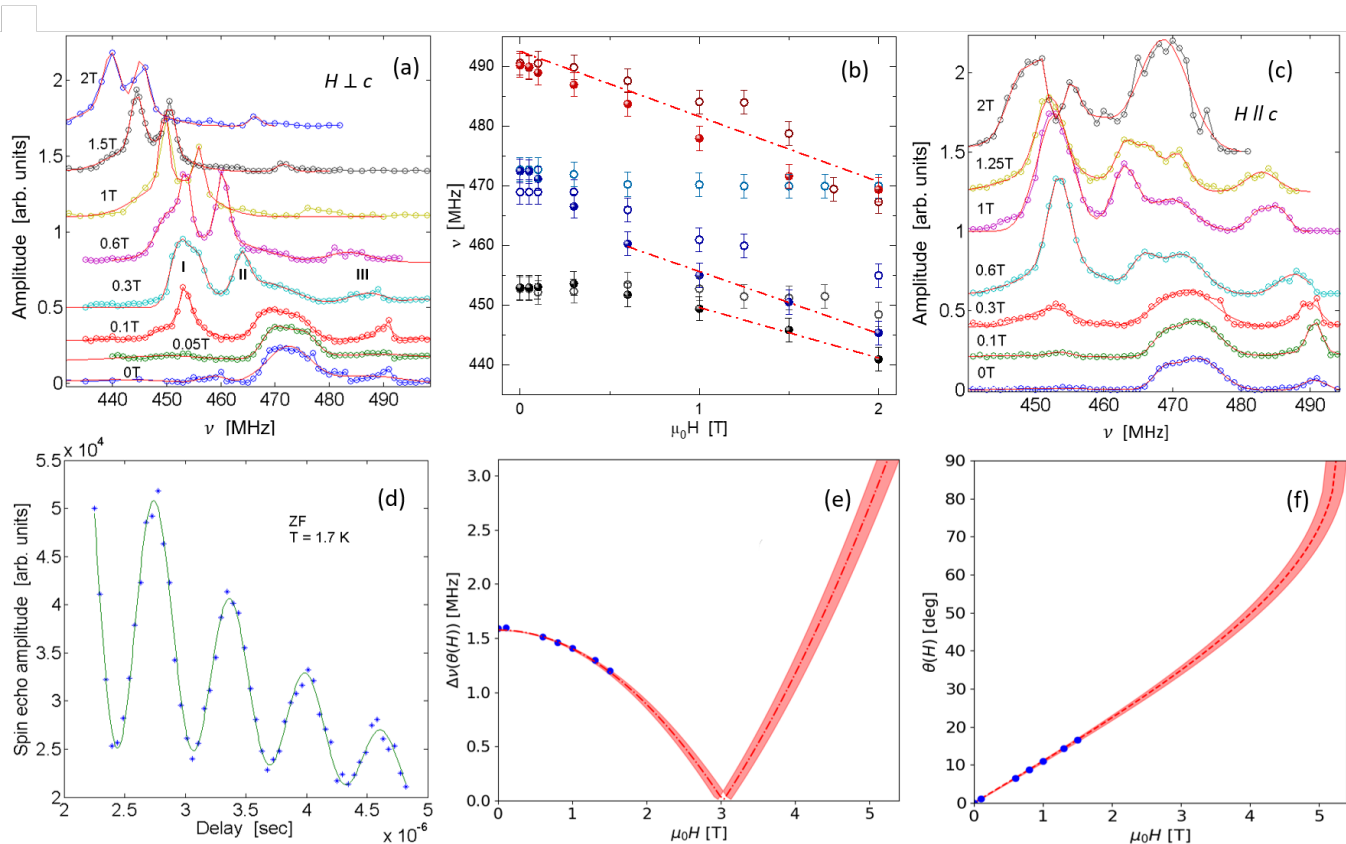


FIG. 6. $\text{Mn}_{1/3}\text{NbS}_2$ single crystal ^{55}Mn NMR in zero and applied fields (a) spectra in $\mathbf{H} \perp \hat{c}$; (b) field dependence of the frequencies center of gravity, for $\mathbf{H} \perp \hat{c}$ (full symbols) and $\mathbf{H} \parallel \hat{c}$ (open symbols); (c) spectra in $\mathbf{H} \parallel \hat{c}$; (d) spin echo amplitude vs. pulse delay at $T = 1.7$ K, $\mu_0 H = 0$ T, 472 MHz displaying oscillations, with solid line best fit to Eq. 12; (e) quadrupole splitting $|\Delta\nu(\theta(H))|$ and (f) conical angle $\theta(H)$ vs. field, from spin-echo oscillation frequency, curves and red bands represent best fit to the absolute value of Eq. 3 with Eq. 4 and their standard deviation, respectively.

peak II, shown in Fig. 6 (d), displaying large amplitude oscillations with a relaxing envelope. This behavior deviates considerably from the normal simple exponential echo decay. The oscillations are observed in ZF and in moderate fields in both peaks I and II of $\text{Mn}_{1/3}\text{NbS}_2$. [31]. This is a well known phenomenon, [33] that arises, in the present context, from coherent beatings of pairs of quadrupole lines originating from the same individual nuclear spin, as explained in more detail in Sec. IV.

All the lines in each multiplet are separated by the same ^{55}Mn quadrupole splitting $\Delta_1(\theta)$ (Eq. 3), which depends on the spin angle $\theta = \theta(H)$. The field dependence can be fitted assuming the monoaxial helical chiral model of Ref. [30] and Eq. 4 for $\theta(H)$ to obtain Fig. 6 (e) and (f). The good quality of both fits confirms at the same time the attribution of the lower frequency majority components to $\text{Mn}_{1/3}\text{NbS}_2$ and the validity of the conical model ($\mathbf{H} \parallel \hat{c}$) for this sample as well. The best-fit parameters are a quadrupole frequency $\nu_Q = 3.15(5)$ MHz and a critical field $\mu_0 H_c = 5.0(5)$ T for the FFM phase which coincides with the saturation field measured in isothermal magnetization, shown in Fig. S3 [31]. Mis-

alignment uncertainties [31] are expected to be the same as for the Cr crystal, of order 5 degrees, and are included in the error estimate. Notice that T_2 oscillations are lost well before reaching this field value.

E. DFT calculations

Ab initio simulations have been performed with a full potential formalism in order to determine both the EFG and the hyperfine field at the Cr and Mn nuclei. The Elk code has been used to perform all simulations and the details are provided in the SI. The experimental lattice structure has been used for all simulations and a ferromagnetic ground state has been used to approximate the long-wavelength helical order. The resulting ground state magnetic moment is $3\mu_B/\text{Cr}$ and $4.2\mu_B/\text{Mn}$ for $\text{Cr}_{1/3}\text{NbS}_2$ and $\text{Mn}_{1/3}\text{NbS}_2$ respectively. Details are given in Sec. IV.

1. DFT in the Cr compound

The EFG has the principal axis for the largest component aligned with the c lattice parameter, and $\eta = 0$ for Cr. We obtain $V_{zz} = 2.2 \times 10^{21}$ V/m² that results in a predicted quadrupole frequency, defined in Eq. 6 $\nu_Q = 4.0$, that compares very well with the experimental estimate provided in Tab. II and agrees with previous reports [34]. The dominant contribution to the hyperfine field is of contact origin and its estimated value is ≈ 13 T. The pseudo-dipolar and orbital contributions are about one order of magnitude smaller and are close to the accuracy limit of the present computational analysis. The final prediction, which includes contact, orbital, and dipolar interactions, results in 16 T, thus underestimating the experimental value of Tab. II by 36%, probably due to numerically limited estimation of orbital and dipolar terms.

2. DFT in the Mn compound

Also in this case the largest component of the EFG tensor is aligned with c and we obtained $V_{zz} = 2.9 \times 10^{21}$ V/m², which results in $\nu_Q = 3.5$ MHz, which compares well with the experimental $\nu_Q = 2|\Delta\nu_1(0)| = 3.15(5)$ MHz. The hyperfine parameters are dominated by the contact part also in this case, which is found to be 20 times larger than orbital and dipolar contributions, which are therefore neglected in the following discussion. The contact field is predicted to be 34.5 T, in perfect agreement with the experimentally observed value.

III. DISCUSSION AND CONCLUSIONS

A. Cr_{1/3}NbS₂

Let us start from the textbook Cr sample, where we detect a ⁵³Cr quadrupole triplet pattern, obscured in previous polycrystal data [27] probably owing to sample quality, but in line with more recent Cr_{1/3}NbSe₂ results [26, 35], indicating that our crystal belongs to the $P6_322$ space group.

The on-site hyperfine field yields an estimate of the Cr magnetic moment of $2.6 \mu_B$ at $T = 0, H = 0$, with a 13% reduction over the spin-only Cr³⁺ value of $3 \mu_B$. Although older magnetization data [36] report a value of $2.9 \mu_B$ at 2 T, our result is in line with the observed T_m 111K and critical field value $\mu_0 H_c = 1.35(1)$ T in our crystal, Fig. 2 (b).

A small non vanishing moment on Nb of order 0.1-0.15 μ_B , opposite to that of Cr is demonstrated by the ⁹³Nb hyperfine field, Fig. 4 and the field dependence of the spectra, Fig. 5. DFT predicts this moment, due to Nb-Cr hybridization, together with a Cr moment closer to the spin-only value.

DFT calculation of the EFG tensor show that its principal component, V_{zz} , is along \hat{c} and orthogonal to \mathbf{B}_{hf} in ZF, establishing that the splitting of the $m = \pm 1$ satellites is the quadrupole frequency of Tab. II [26].

A prior study [24] indicates that $\mathbf{H} \perp \hat{c}$ generates the expected 2π domain walls corresponding to magnetic solitons (CSL), giving way to the FFM phase around $\mu_0 H = 40$ mT. In our data this is a tiny field compared to the substantial $B_{hf} = 25$ T, barely showing up as a flattening of the shifts (Fig. 1 (b) towards $H = 0$).

The transition of the CHM to the CCP by applying the field along the chiral axis ($\mathbf{H} \parallel \hat{c}$) is neatly witnessed by the fit of Fig. 2 (a), and the simultaneous agreement of the extracted conical angle $\theta(H)$ of panel (b) with the mean-field theory. [10] This provides a precise measurement of the boundary to the FFM phase, $\mu_0 H_c = 1.35(1)$ T, albeit for a sample that has a sub-optimal T_m . The fit deviation of the point at $\mu_0 H = 40$ mT, which coincides within errorbars with the ZF value, demonstrates the presence of a pinned CHM phase at low fields in our crystal, i.e. of a small coercive field required to initiate the spin canting. The very fine agreement of the canted model also establishes the model of the joint Eqs. 2 and 4 as a strong validation of the presence of the conical phase.

The first-order nature of the transition at T_m is very clearly shown by NMR, a local probe which can separate the decrease of the magnetic phase volume from that of the moment, a distinction that neither diffraction nor macroscopic techniques can easily operate. This finding is consistent with mean field predictions [37] and a previous analysis of the entropy change at the transition [38] in a work that attributes the difficulty of measuring this change to a weak first-order nature. The NMR convincing signature is a more direct assessment of the same fact.

The vector addition of the external and internal fields at ⁹³Nb demonstrated that the Nb spin is opposite to that of Cr, as in the the spin structure suggested in Ref. [35], which is shown in Fig. 7.

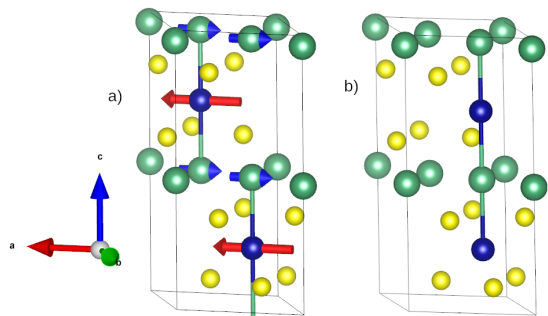


FIG. 7. a) Spin structure in Cr_{1/3}NbS₂, including the small magnetic moment on Nb (not to scale); b) stacking fault along \hat{c} .

The refined fit of the polycrystalline sample (orange curves in Fig. 4) requires an additional 6% of the Nb nu-

clei in defect sites, with minority 2c Wyckoff site occupancy (see Sec. IV). Also the broader, asymmetric polycrystalline ^{53}Cr triplet lineshapes (not shown) agree with a small percentage of such defect sites, not observed in the single crystal.

In summary, we may classify the ^{53}Cr NMR data from our single crystal and polycrystal samples as a textbook case for an ideal monoaxial chiral helimagnet.

B. $\text{Mn}_{1/3}\text{NbS}_2$

Our more interesting findings are on the Mn compound, whose magnetic phase diagram [24] is still lacking a precise identification. The three component NMR spectra are assigned to a minority $\text{Mn}_{1/4}\text{NbS}_2$ inclusion and to two structural variations of the dominant $\text{Mn}_{1/3}\text{NbS}_2$ phase.

A previous work [24] has shown a partial occupation of the Mn 2b site in the very same samples used in this work. First principles simulations show that the additional Mn moment is slightly reduced (by $\sim 2.5\%$) and aligned antiparallel to its three neighbouring Mn 3c atoms. Its presence reflects on the neighbouring Mn atoms as well, by producing a similar reduction of their local magnetic moment, and it may be qualitatively justified by opposite signs of the on-site and transferred hyperfine couplings for the nn sites (Sec. IV B). The reduction compares reasonably well with the experimental ratio $(^{55}\nu_{II} - ^{55}\nu_I)/^{55}\nu = 0.043$, thus assigning component I to the ^{55}Mn nuclei with one nearest neighbor (nn) 2b site and component II to the less perturbed, more removed nuclei. A simple binomial simulation of the 2b, d Mn sites nn to 2c, assuming the refined occupancies of Ref. [24] (0.85, 0.08 and 0.02 for Mn sites 2c, 2b, and 2d respectively) indicates that two main environments are most probable: those with no nn defects ($p = 0.73$) and those with one nn defect of either 2b or 2d type ($p = 0.24$). This supports our observation of two groups of resonances in single crystal $\text{Mn}_{1/3}\text{NbS}_2$ in Fig. 6.

This qualitative attribution is confirmed by the behavior of the quadrupole splitting observed through the well known mechanism of spin echo oscillations shown in Fig. 6 (d). The successful fit for $\mathbf{H} \parallel \hat{c}$ to Eq. 12 is plotted in Fig 6 (e), (f) and supports the chiral conical model. The success relies on the homogeneity of the quadrupole coupling for all nuclei, despite the disorder-induced, broad magnetic inhomogeneous distribution of hyperfine fields, which hampers a better refinement of the ^{55}Mn NMR spectrum. In addition, the first moment of the two low frequency ^{55}Mn components in Fig. 6 (b) is also compatible with the same model, despite the disorder: the negative slopes agree with $^{55}\gamma$ for $\mathbf{H} \perp \hat{c}$ and a much reduced initial field dependence is observed for $^{55}\gamma$ for $\mathbf{H} \parallel \hat{c}$, like in the ^{53}Cr case. This peculiar behavior, leading to very different onset fields for the FFM phase in the two orientations, also clearly identifies the majority phase as a chiral helical magnet, with rather

larger phase boundaries to the forced ferromagnet phase, in agreement with magnetometry data [31].

C. Conclusions

We have shown that $\text{Cr}_{1/3}\text{NbS}_2$ is a textbook case of a chiral monoaxial helimagnet, and we have improved the determination of its CCP to FFM phase boundary at $T = 0$. This allowed us to establish a very detailed model for the NMR of a CHM, and leveraging on this we have further shown that, despite the much higher degree of intrinsic disorder, $\text{Mn}_{1/3}\text{NbS}_2$ also fully qualifies as a chiral helical magnet.

IV. METHODS

A. Samples

Polycrystalline and single crystal samples of $\text{Cr}_{1/3}\text{NbS}_2$ and $\text{Mn}_{1/3}\text{NbS}_2$ studied in this work were synthesized by solid-state reaction and chemical vapor transport techniques, respectively, using the procedures described in [24]. Single crystals in the form of platelets approximately 3 mm along the longest edge were obtained. The phase purity of the polycrystalline materials was checked using X-ray powder diffraction. Single crystal x-ray diffraction was used to ascertain the non-centrosymmetric space group. Laue x-ray back-reflection studies were carried out to establish the crystalline quality as well as to check the crystallographic orientations of the obtained single crystals.

B. NMR and NQR

In the ordered magnetic phase, the full spin Hamiltonian for the nuclear spin I is [39]

$$\begin{aligned} \mathcal{H} &= \mathcal{H}_Z + \mathcal{H}_Q \\ &= h\gamma(\mu_0\mathbf{H} + \mathbf{B}_{\text{hf}}) \cdot \mathbf{I} + \frac{h\nu_Q}{3V_{zz}}\mathbf{I} \cdot \mathbf{V} \cdot \mathbf{I}, \end{aligned} \quad (5)$$

$$\nu_Q = \frac{3eV_{zz}Q}{2I(2I-1)\hbar}. \quad (6)$$

For both compounds and all three nuclei considered here the hierarchy is always $\mathcal{H}_Z > \mathcal{H}_Q$, hence the quantization axis is that of \mathbf{B}_{hf} , which may be rotated by the application of \mathbf{H} .

We assume that the coupling tensors in the ideal structure are nearly cylindrical, with principal axis z along \hat{c} , the EFG tensor asymmetry parameter $\eta = (V_{xx} - V_{yy})/V_{zz} \approx 0$ and $B_{\text{hf}}^x \approx B_{\text{hf}}^y$, justifying Eqs. 1-3, in agreement with both the best fits and the DFT predictions (Sec. II E).

The conventional description of the static hyperfine field is

$$\mathbf{B}_{\text{hf}} = \mathcal{A} \cdot \mathbf{S} + \sum_{\langle j \rangle} \mathcal{B}_j \mathbf{S}_j, \quad (7)$$

where \mathcal{A} is the nearly isotropic on-site term, the index $\langle j \rangle$ runs over nearest neighbor magnetic moment and the term \mathcal{B}_j is their transferred coupling, mediated by \mathbf{S} . We ignore the transferred hyperfine coupling to second nearest neighbor (nn) 3d ions, and also the coupling to nn Nb, in view of the small moment due to the Cr-Nb hybridization. In the case of Cr at the 2c Wyckoff site, with nearly zero occupancy of nearest neighbor 2b, d sites, this amounts to keeping only the on-site term. The Mn case is discussed in Sec. III B.

C. ^{93}Nb NMR fit

The model for the simulation of the Nb spectrum, described in Sec. IV C, is implemented in the fit of Fig. 4 (gray dashed curve). The best fit is close to the data and the peak positions are almost correct, but deviations are evident from the residues. An extremely good fit (orange solid curve, compare also the residues) includes a second pair of sites, as shown in Tab. III, of small total amplitude and much broader magnetic inhomogeneity. The defect is consistent with a single Cr atom at the predominantly empty 2b or 2d Wyckoff sites. The interpretation is supported by the much larger width of the satellites in these two components, indicative of a magnetically more disordered local condition, i.e. many similar, slightly different configurations due to more distant defects.

In the basic 2-site model for ^{93}Nb ZF-NMR the ratio of the 2a and 2b site amplitudes is fixed to 1:2. The Gaussian width is common to all the satellites of a site, as it is expected for inhomogeneity of magnetic origin. The magnetic moment is $\mathbf{S} \perp c$, yielding a magnetic field in the same direction. In this orientation the second-order quadrupole-perturbed frequencies (a better approximation than that of Eqs. 6-8) for the semi-integer nuclear spin $I = \frac{9}{2}$ are

$$\nu_m = \nu_{\text{hf}} + m \frac{\nu_{\text{Q}}}{2} + \frac{3\nu_{\text{Q}}^2}{2\nu_{\text{hf}}} \left(1 - \frac{m^2}{8} \right), \quad (8)$$

where $m = -\frac{2I-1}{2}, \dots, \frac{2I-1}{2}$ is the satellite order. This fit, shown in Fig. 4 by the gray curve and residues, produces nine resonance satellites for each inequivalent Nb site, optimized by as many Gaussian terms, with amplitudes scaling as

$$\left| \left\langle m - \frac{1}{2} | I_x | m + \frac{1}{2} \right\rangle \right|^2 = \frac{I(I+1) - m^2 + \frac{1}{4}}{4}. \quad (9)$$

The best fit is the orange curve in Fig. 4 and its parameters are displayed in Tab. IV.

TABLE IV. ^{93}Nb quadrupolar and hyperfine parameter of the 4-site best fit (Eqs. 8,9) shown in Fig. 4).

Wyckoff site	pair fraction	ν_{Q} [MHz]	ν_{hf} [MHz]	$\delta\nu$ [MHz]
2a ₁	0.94	0.83	8.82	0.15
2b ₁		1.2	13.8	0.11
2a ₂	0.06	1.8	10.7	0.74
2b ₂		0.9	14.9	0.65

In the 4-site model the parameters of the majority pair are very similar to those of the simpler 2-site fit. The second pair has the same fixed amplitude ratio, a much smaller total area and broader satellite widths. This second pair represents a marginal fraction of ^{93}Nb close to a defect; the presence of the defect results in ^{93}Nb hyperfine field and quadrupole frequency ratios $2a_2/2a_1$ (and $2b_2/2b_1$) of 1.22 (1.08) and 2.20 (0.73), respectively. The defect site is tentatively attributed to Cr at the 2b, d sites, marginally present in the powders and virtually absent in the single crystal.

D. NMR experiments

The NMR spectra were acquired utilizing the HyReSpect home-built phase coherent broadband spectrometer [40] equipped with a 9T magnet and a He-flow sample insert. The very broad spectra were recorded point by point at each frequency, in a Hahn spin-echo refocusing pulse sequence, P- τ -P. The P pulse duration and intensity were optimized for maximum signal, with the shortest τ delay, constrained by the apparatus dead time of a few microseconds. Spectra were reconstructed from the spin-echo Fourier transform amplitude at each frequency, adjusted for frequency-dependent sensitivity, and the nuclear Boltzmann factor, corrected for the T_2^{-1} relaxation rates obtained by fitting the same spin-echo amplitude vs. delay (2τ) to a relaxation function (exponential decay or Eq. 12). Peaks in the spectra were assigned to each quadrupole transition (^{53}Cr), or each hyperfine component (^{55}Mn), here generically labeled α . The best fit of each peak often requires more than one Gaussian component,

$$G_{\alpha}(\nu) = \sum_{i=1}^n \frac{A_{\alpha,i}}{\sqrt{2\pi}\sigma_{\alpha,i}} \exp \left[-\frac{1}{2} \left(\frac{\nu - \nu_{\alpha,i}}{\sigma_{\alpha,i}} \right)^2 \right], \quad (10)$$

whose mean frequency was computed as its first-moment $\overline{\nu}_{\alpha}$ by the weights $w_{\alpha,i}$:

$$\overline{\nu}_{\alpha} = \sum_i w_{\alpha,i} \nu_{\alpha,i}, \quad w_{\alpha,i} = \frac{A_{\alpha,i}}{\sum_k A_{\alpha,k}}. \quad (11)$$

The ZF and very low field nuclear spin echoes were measured using a non-resonant probe circuit under a substantial radio-frequency (rf) enhancement $\eta_{\text{rf}} = H_1^*/H_1$,

where H_1 is the applied field at the rf ω , and H_1^* is the response, the induced ω oscillating component of the large hyperfine field. [41, 42]. The enhancement is progressively suppressed by the increasing applied fields, requiring the use of a tunable resonant probe.

The coherent oscillations in the spin echo relaxation amplitude vs. delay time 2τ , [33, 43, 44], (Fig. 6d and Fig. S.1) originate from irradiating a broad spectrum, due to an inhomogeneous distribution of interactions (i.e., changing from nucleus to nucleus), in the presence of a smaller, more coherent interaction (i.e. the same for all nuclei). The coherent interaction determines a frequency splitting on each nucleus. If the rf spectral width is broader than the splitting, the echo amplitude includes the beating envelope of the two components as an oscillation. A general expression is

$$A(\tau) = [A_0 + A_1 \cos(4\pi\Delta\nu_0\tau) + \phi] \exp\left(-\frac{2\tau}{T_1}\right). \quad (12)$$

Here, the quadrupole $\Delta\nu_0(H)$ of Eq. 3 plays the coherent splitting role and the inhomogeneous broadening is magnetic.

E. Density Functional Theory

Ab initio simulations based on DFT have been performed with a Full Potential approach using the augmented plane waves basis for the prediction of EFGs while a plane wave basis set has been used to run a supercell simulation reproducing the presence of a fractional occupation of the Mn $2b$ site in $\text{Mn}_{1/3}\text{NbS}_2$. For the first set of simulations, the Elk code was used [45]. A ferromagnetic ground state is used to approximate the long-wavelength helical magnetic ground state. The description of core electrons is obtained with the spin polarized solution to the Dirac equation under the influence of valence electrons' spin polarization. This allows us to correctly describe the induced core orbital polarization that represents a sizable contribution to hyperfine fields. For these simulations we considered spin-orbit coupling and converged the number of empty states used for the second-variational step in the iterative solution of Khon-Sham equations. A $8 \times 8 \times 4$ Monkhorst-Pack grid is used to sample reciprocal space and the default parameters define the basis set. For additional details, such as

the input and output files, see [46]. For the exchange and correlation contributions we adopt the PBE functional [47].

For plane wave based simulations aimed at describing the role of Mn in the $2b$ site we used the QuantumESPRESSO suite of codes [48–50]. In this case we did not include spin-orbit coupling and ultrasoft pseudopotentials were taken from the GBRV pseudopotential library (version 1.5). A single additional Mn atom in the $2b$ site is placed in a $3 \times 3 \times 1$ supercell containing 181 atoms. A Monkhorst-Pack $2 \times 2 \times 2$ grid is used to sample the reciprocal space. The structure is relaxed considering both an initial magnetization for Mn $2b$ parallel or antiparallel to that of the other manganese site. The antiparallel alignment is about 0.2 eV lower in energy.

V. DATA AVAILABILITY

The original data in this work is available at the Archive Material Cloud. [46]

VI. DECLARATION OF COMPETING INTEREST

The authors declare that they have no known competing financial interests or personal relationships that could have appeared to influence the work reported in this paper.

VII. ACKNOWLEDGMENTS

This work was supported by the Deutsche Forschungsgemeinschaft (DFG) within the Würzburg-Dresden Cluster of Excellence on Complexity and Topology in Quantum Matter – *ct.qmat* (EXC 2147, project-id 390858490) and the SFB 1143 (project-id 247310070). Work in Parma was funded by the PNRR MUR project ECS-00000033-ECOSISTER. The computational resources were provided by the SCARF cluster of the STFC Scientific Computing Department and by the ISCRA initiative of CINECA with project IsCb6_TRSBKS. The work at the University of Warwick was funded by EPSRC, UK through Grants EP/T005963/1 and EP/N032128/1.

[1] W. Choi, N. Choudhary, G. H. Han, J. Park, D. Akinwande, and Y. H. Lee, Recent development of two-dimensional transition metal dichalcogenides and their applications, *Materials Today* **20**, 116 (2017).
 [2] S. Manzeli, D. Ovchinnikov, D. Pasquier, O. V. Yazyev, and A. Kis, 2d transition metal dichalcogenides, *Nature Reviews Materials* **2**, 1 (2017).

[3] Z. Wei, B. Li, C. Xia, Y. Cui, J. He, J.-B. Xia, and J. Li, Various structures of 2d transition-metal dichalcogenides and their applications, *Small Methods* **2**, 1800094 (2018).
 [4] A. Krasnok, S. Lepeshov, and A. Alú, Nanophotonics with 2d transition metal dichalcogenides, *Optics express* **26**, 15972 (2018).
 [5] K. F. Mak and J. Shan, Photonics and optoelectronics of 2d semiconductor transition metal dichalcogenides, *Nature*

- ture Photonics **10**, 216 (2016).
- [6] S. Parkin and R. Friend, 3 d transition-metal intercalates of the niobium and tantalum dichalcogenides. i. magnetic properties, Philosophical Magazine B **41**, 65 (1980).
- [7] R. Friend, A. Beal, and A. Yoffe, Electrical and magnetic properties of some first row transition metal intercalates of niobium disulphide, The Philosophical Magazine: A Journal of Theoretical Experimental and Applied Physics **35**, 1269 (1977).
- [8] M. Mito, H. Ohsumi, T. Shishidou, F. Kuroda, M. Weinert, K. Tsuruta, Y. Kotani, T. Nakamura, Y. Togawa, J. Kishine, *et al.*, Observation of orbital angular momentum in the chiral magnet CrNb_3S_6 by soft x-ray magnetic circular dichroism, Physical review B **99**, 174439 (2019).
- [9] A. E. Hall, D. D. Khalyavin, P. Manuel, D. A. Mayoh, F. Orlandi, O. A. Petrenko, M. R. Lees, and G. Balakrishnan, Magnetic structure investigation of the intercalated transition metal dichalcogenide $\text{V}_{1/3}\text{NbS}_2$, Phys. Rev. B **103**, 174431 (2021).
- [10] Y. Kousaka, Y. Nakao, J.-i. Kishine, M. Akita, K. Inoue, and J. Akimitsu, Chiral helimagnetism in $\text{tTl}/3\text{NbS}_2$ ($t = \text{Cr}$ and Mn), Nuclear Instruments and Methods in Physics Research Section A: Accelerators, Spectrometers, Detectors and Associated Equipment **600**, 250 (2009).
- [11] Y. Kousaka, T. Ogura, J. Zhang, P. Miao, S. Lee, S. Torii, T. Kamiyama, J. Campo, K. Inoue, and J. Akimitsu, Long periodic helimagnetic ordering in CrMn_3S_6 ($m = \text{Nb}$ and Ta), in *Journal of Physics: Conference Series*, Vol. 746 (IOP Publishing, 2016) p. 012061.
- [12] Y. Togawa, T. Koyama, K. Takayanagi, S. Mori, Y. Kousaka, J. Akimitsu, S. Nishihara, K. Inoue, A. Ovchinnikov, and J.-i. Kishine, Chiral magnetic soliton lattice on a chiral helimagnet, Physical review letters **108**, 107202 (2012).
- [13] D. Braam, C. Gomez, S. Tezok, E. de Mello, L. Li, D. Mandrus, H.-Y. Kee, and J. Sonier, Magnetic properties of the helimagnet $\text{Cr}/3\text{NbS}_2$ observed by μ sr, Physical Review B **91**, 144407 (2015).
- [14] Y. Dai, W. Liu, Y. Wang, J. Fan, L. Pi, L. Zhang, and Y. Zhang, Critical phenomenon and phase diagram of Mn -intercalated layered MnNb_3S_6 , Journal of Physics: Condensed Matter **31**, 195803 (2019).
- [15] S. K. Karna, F. Womack, R. Chapai, D. Young, M. Marshall, W. Xie, D. Graf, Y. Wu, H. Cao, L. DeBeer-Schmitt, *et al.*, Consequences of magnetic ordering in chiral $\text{Mn}/3\text{NbS}_2$, Physical Review B **100**, 184413 (2019).
- [16] D. A. Mayoh, J. Bouaziz, A. E. Hall, J. B. Staunton, M. R. Lees, and G. Balakrishnan, Giant topological and planar hall effect in $\text{Cr}_{1/3}\text{NbS}_2$, Phys. Rev. Res. **4**, 013134 (2022).
- [17] N. L. Nair, E. Maniv, C. John, S. Doyle, J. Orenstein, and J. G. Analytis, Electrical switching in a magnetically intercalated transition metal dichalcogenide, Nature materials **19**, 153 (2020).
- [18] S. Okumura, H. Ishizuka, Y. Kato, J.-i. Ohe, and Y. Motome, Spin-current diode with a monoaxial chiral magnet, Applied Physics Letters **115** (2019).
- [19] F. Boswell, A. Prodan, W. Vaughan, and J. Corbett, On the ordering of Fe atoms in FeNbS_2 , physica status solidi (a) **45**, 469 (1978).
- [20] F. Hulliger and E. Pobitschka, On the magnetic behavior of new 2H-nbS_2 -type derivatives, Journal of Solid State Chemistry **1**, 117 (1970).
- [21] V. Dyadkin, F. Mushenok, A. Bosak, D. Menzel, S. Grigoriev, P. Pattison, and D. Chernyshov, Structural disorder versus chiral magnetism in $\text{Cr}/3\text{NbS}_2$, Physical Review B **91**, 184205 (2015).
- [22] R. Aoki, Y. Kousaka, and Y. Togawa, Anomalous non-reciprocal electrical transport on chiral magnetic order, Physical Review Letters **122**, 057206 (2019).
- [23] A. A. Bykov, N. Chubova, E. Altinbaev, Y. Kousaka, A. Ovchinnikov, J. Kishine, and S. Grigoriev, Magnetic phase diagram of $\text{Cr}/3\text{NbS}_2$: Sans study, Journal of Solid State Chemistry **322**, 123951 (2023).
- [24] A. Hall, J. Loudon, P. Midgley, A. Twitchett-Harrison, S. Holt, D. Mayoh, J. Tidey, Y. Han, M. R. Lees, and G. Balakrishnan, Comparative study of the structural and magnetic properties of $\text{Mn}/3\text{NbS}_2$ and $\text{Cr}/3\text{NbS}_2$, Physical Review Materials **6**, 024407 (2022).
- [25] S. K. Karna, M. Marshall, W. Xie, L. DeBeer-Schmitt, D. P. Young, I. Vekhter, W. A. Shelton, A. Kovács, M. Charilaou, and J. F. DiTusa, Annihilation and control of chiral domain walls with magnetic fields, Nano letters **21**, 1205 (2021).
- [26] V. Ogloblichev, Y. V. Piskunov, and F. Mushenok, Magnetic order in the structurally disordered helicoidal magnet $\text{Cr}/3\text{NbS}_2$: Nmr at 53 Cr nuclei, Journal of Experimental and Theoretical Physics **125**, 317 (2017).
- [27] V. Ogloblichev, Y. V. Piskunov, I. Y. Arapova, and F. Mushenok, The valence state of manganese in the $\text{Mn}/3\text{NbS}_2$ magnet according to 55 Mn-nmr data, Physics of Metals and Metallography **119**, 1056 (2018).
- [28] W. Ertmer, U. Johann, and R. Mosmann, Measurement of the nuclear quadrupole moment of ^{53}Cr by laser-rf double resonance, Z. Phys. A - Atoms and Nuclei **309** (1982).
- [29] D. Stephenson and N. Singh, ^{53}Cr , ^{17}O and ^{14}N nuclear quadrupole resonance in ammonium dichromate, Hyperfine Interact. **237**, 118 (2016), <https://doi.org/10.1007/s10751-016-1332-3>.
- [30] J.-I. Kishine and A. Ovchinnikov, Theory of monoaxial chiral helimagnet, Solid State Physics **66**, 1 (2015).
- [31] Supplemental Material, Supplemental Material.
- [32] A. Rahman, M. U. Rehman, M. Yousaf, M. Kiani, H. Zhao, J. Wang, Y. Lu, K. Ruan, R. Dai, Z. Wang, *et al.*, Rkky-type in-plane ferromagnetism in layered $\text{Mn}/4\text{NbS}_2$ single crystals, Physical Review B **105**, 214410 (2022).
- [33] H.-A. Krug von Nidda, N. Büttgen, and A. Loidl, Magnetic resonance in quantum spin chains, The European Physical Journal Special Topics **180**, 161 (2010).
- [34] P. Agzamova and V. Ogloblichev, Electronic structure and hyperfine interactions in Cr_xNbSe_2 ($x = 0.33, 0.5$) by dft studies, Applied Magnetic Resonance **54**, 439–448 (2022).
- [35] V. Ogloblichev, N. Baranov, P. Agzamova, A. Y. Gernov, N. Nosova, Y. V. Piskunov, E. Sherokalova, N. Selezneva, A. Sadykov, and A. Smolnikov, Electronic states in ferromagnetic Cr_xNbSe_2 ($x = 0.33, 0.5$) studied by Cr 53 and Nb 93 nmr spectroscopy, Physical Review B **104**, 245115 (2021).
- [36] T. Miyadai, K. Kikuchi, H. Kondo, S. Sakka, M. Arai, and Y. Ishikawa, Magnetic properties of $\text{Cr}/3\text{NbS}_2$, Journal of the Physical Society of Japan **52**, 1394 (1983), <https://doi.org/10.1143/JPSJ.52.1394>.
- [37] V. Laliena, J. Campo, and Y. Kousaka, Understanding the $h-t$ phase diagram of the monoaxial helimagnet, Phys. Rev. B **94**, 094439 (2016).

- [38] E. M. Clements, R. Das, L. Li, P. J. Lampen-Kelley, M.-H. Phan, V. Keppens, D. Mandrus, and H. Srikanth, Critical behavior and macroscopic phase diagram of the monoaxial chiral helimagnet $\text{Cr}_1/3\text{NbS}_2$, *Scientific reports* **7**, 6545 (2017).
- [39] A. Abragam, *The principles of nuclear magnetism*, Vol. 32 (Oxford University Press, 1961) international Series of Monographs on Physics.
- [40] G. Allodi, A. Banderini, R. De Renzi, and C. Vignali, Hyrespect: a broadband fast-averaging spectrometer for nuclear magnetic resonance of magnetic materials, *Review of scientific instruments* **76** (2005).
- [41] A. Sidorenko, G. Allodi, R. De Renzi, G. Balestrino, and M. Angeloni, Mn 55 nmr and magnetization studies of the $\text{La}_2\text{O}_3/\text{Sr}_2\text{O}_3$ thin films, *Physical Review B* **73**, 054406 (2006).
- [42] C. Meny and P. Panissod, Nuclear magnetic resonance in ferromagnets: Ferromagnetic nuclear resonance; a very broadband approach, in *Annual Reports on NMR Spectroscopy*, Vol. 103 (Elsevier, 2021) pp. 47–96.
- [43] H. Abe, H. Yasuoka, and A. Hirai, Spin echo modulation caused by the quadrupole interaction and multiple spin echoes, *Journal of the Physical Society of Japan* **21**, 77 (1966).
- [44] A. Lombardi, M. Mali, J. Roos, and D. Brinkmann, Hyperfine fields at the Ba site in the antiferromagnet $\text{YBa}_2\text{Cu}_3\text{O}_{6.05}$, *Phys. Rev. B* **53**, 14268 (1996).
- [45] Elk code, <https://elk.sourceforge.io/>, accessed: 2024-08-13.
- [46] M. Sahoo, P. Bonfà, A. E. Hall, D. A. Mayoh, L. T. Corredor, A. U. B. Wolter, B. Büchner, G. Balakrishnan, R. De Renzi, and G. Allodi, Disorder-resilient transition of helical to conical ground states in $\text{m}_{1/3}\text{NbS}_2$, $\text{m}=\text{Cr}, \text{Mn}$.
- [47] J. P. Perdew, K. Burke, and M. Ernzerhof, Generalized gradient approximation made simple, *Phys. Rev. Lett.* **77**, 3865 (1996).
- [48] P. Giannozzi, O. Basergio, P. Bonfà, D. Brunato, R. Car, I. Carnimeo, C. Cavazzoni, S. de Gironcoli, P. Delugas, F. Ferrari Ruffino, A. Ferretti, N. Marzari, I. Timrov, A. Urru, and S. Baroni, Quantum espresso toward the exascale, *The Journal of Chemical Physics* **152**, 154105 (2020), <https://doi.org/10.1063/5.0005082>.
- [49] P. Giannozzi, O. Andreussi, T. Brumme, O. Bunau, M. B. Nardelli, M. Calandra, R. Car, C. Cavazzoni, D. Ceresoli, M. Cococcioni, N. Colonna, I. Carnimeo, A. D. Corso, S. de Gironcoli, P. Delugas, R. A. D. Jr, A. Ferretti, A. Floris, G. Fratesi, G. Fugallo, R. Gebauer, U. Gerstmann, F. Giustino, T. Gorni, J. Jia, M. Kawamura, H.-Y. Ko, A. Kokalj, E. Küçükbenli, M. Lazzeri, M. Marsili, N. Marzari, F. Mauri, N. L. Nguyen, H.-V. Nguyen, A. O. de-la Roza, L. Paulatto, S. Poncè, D. Rocca, R. Sabatini, B. Santra, M. Schlipf, A. P. Seitsonen, A. Smogunov, I. Timrov, T. Thonhauser, P. Umari, N. Vast, X. Wu, and S. Baroni, Advanced capabilities for materials modelling with quantum espresso, *Journal of Physics: Condensed Matter* **29**, 465901 (2017).
- [50] P. Giannozzi, S. Baroni, N. Bonini, M. Calandra, R. Car, C. Cavazzoni, D. Ceresoli, G. L. Chiarotti, M. Cococcioni, I. Dabo, A. Dal Corso, S. de Gironcoli, S. Fabris, G. Fratesi, R. Gebauer, U. Gerstmann, C. Gougoussis, A. Kokalj, M. Lazzeri, L. Martin-Samos, N. Marzari, F. Mauri, R. Mazzarello, S. Paolini, A. Pasquarello, L. Paulatto, C. Sbraccia, S. Scandolo, G. Sclauzero, A. P. Seitsonen, A. Smogunov, P. Umari, and R. M. Wentzcovitch, Quantum espresso: a modular and open-source software project for quantum simulations of materials, *Journal of Physics: Condensed Matter* **21**, 395502 (19pp) (2009).

Supplemental Material, Disorder-resilient transition of Helical to Conical ground states in $M_{1/3}\text{NbS}_2$, $M=\text{Cr},\text{Mn}$.

M. Sahoo,^{1,2,3} P. Bonfá,¹ A. E. Hall,⁴ D. A. Mayoh,⁴ L. T. Corredor,² A. U. B. Wolter,² B. Büchner,^{2,3} G. Balakrishnan,⁴ R. De Renzi,^{1,*} and G. Allodi¹

¹*Dipartimento di Scienze Matematiche, Fisiche ed Informatiche, Università di Parma, Parco Area delle Scienze 7A, I-43124 Parma, Italy*

²*Leibniz IFW Dresden, Helmholtzstraße 20, D-01069 Dresden, Germany*

³*Institut für Festkörper- und Materialphysik and Würzburg-Dresden Cluster of Excellence ct.qmat, Technische Universität Dresden, 01062 Dresden, Germany*

⁴*Department of Physics, University of Warwick, Coventry, CV4 7AL, United Kingdom*

(Dated: October 3, 2024)

I. ⁵⁵MN SPIN ECHO AMPLITUDE OSCILLATIONS

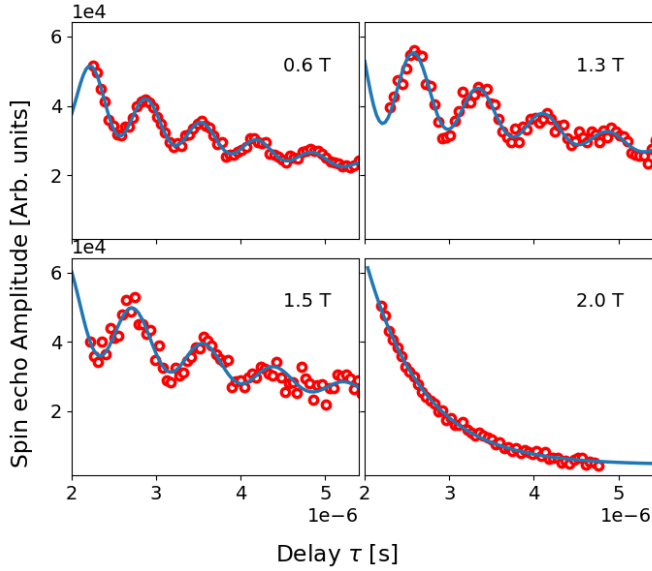


FIG. S.1: ⁵⁵Mn spin echo amplitude vs. delay time 2τ in $\text{Mn}_{1/3}\text{NbS}_2$ at several fields and frequencies, with $\mathbf{H} \parallel \hat{c}$ at $T = 1.7$ K.

Representative spin-echo amplitudes versus spin-echo delay 2τ showing an exponential decay modulated by oscillations are shown in Fig. S.1 for $\mathbf{H} \parallel \hat{c}$ and frequencies around the maximum of the component that peaks at 475 MHz in ZF (component II). Similar oscillations (not shown) are obtained for the spin echo-amplitude of component I. The best fit (solid line) is to Eq. 12 (main paper) The oscillating amplitude, A_1 , decreases with increasing H , disappearing above 2T.

II. MEAN FIELD

The CHS many-body Hamiltonian for $\mu_0\mathbf{H} \parallel \mathbf{D} \parallel \hat{z}$ is

$$\mathcal{H} = \sum_i \left\{ g\mu_B S_z B - \sum_{\langle j \rangle} [J\mathbf{S}_i \cdot \mathbf{S}_j + D(S_{ix}S_{jy} - S_{jx}S_{iy})] \right\}. \quad (1)$$

In the CHS mean field approximation, the mean spin $\langle \mathbf{S}_i \rangle$ has polar angles Θ, Φ whereas its nearest neighbor $\langle j \rangle$ in the direction of $\mathbf{q} \parallel \hat{c}$ has polar angles $\Theta, \Phi + \phi$, therefore the exchange term reads

$$\mathbf{S}_i \cdot \mathbf{S}_j = \begin{cases} S^2 & \perp \hat{c}, \\ S^2(\cos^2 \Theta + \sin^2 \Theta \cos \phi) & \parallel \hat{c}, \end{cases} \quad (2)$$

and the Dzyaloshinskii-Moriya term reads

$$S_{ix}S_{jy} - S_{jx}S_{iy} = \begin{cases} 0 & \perp \hat{c}, \\ S^2 \sin^2 \Theta \sin \phi & \parallel \hat{c}. \end{cases} \quad (3)$$

Hence the mean energy per spin unit with N sites in the lattice and z_\perp, z_\parallel nearest neighbors in the ab plane and along the c axis, respectively

$$\begin{aligned} \langle e \rangle &= \frac{\langle \mathcal{H} \rangle}{NS} = g\mu_B B \cos \Theta \\ &\quad - S [J(z_\perp + z_\parallel(\cos^2 \Theta + \sin^2 \Theta \cos \phi)) \\ &\quad + z_\parallel D \sin^2 \Theta \sin \phi]. \end{aligned} \quad (4)$$

The condition $d\langle e \rangle/d\phi = 0$ yields the mean-field helix pitch, $\tan \phi = D/J \ll 1$, hence $\sin \phi \approx D/J$ and $1 - \cos \phi \approx D^2/2J^2$. Viceversa, the condition $d\langle e \rangle/d\Theta = 0$ yields the Forced Ferromagnetic critical field and the field dependence $\Theta(H)$

$$\begin{aligned} \frac{d\langle e \rangle}{d\Theta} &= -\sin \Theta \\ &\quad [g\mu_B B + 2 \cos \Theta S z_\parallel \\ &\quad (J(1 - \cos \phi) + D \sin \phi)]. \end{aligned} \quad (5)$$

* Corresponding address: roberto.derenzi@unipr.it

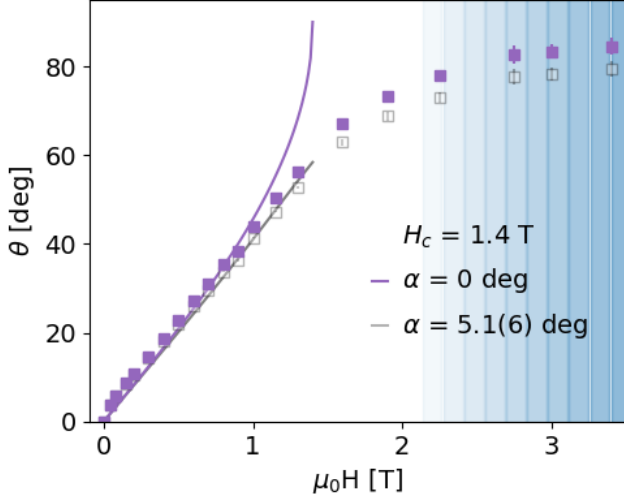


FIG. S.2: Data as in Fig. 3, compared here to two mean-field curves, for perfect alignment (purple, Eq. 6) and for a misalignment of 5.1 degrees (grey, Eq. 7).

Substituting the approximate values for ϕ and defining the coefficient of $\cos \Theta$ as $/g\mu_B\mu_0 H_c \approx -2S z_{\parallel} D^2/2J$ we get either $\Theta = 0$ (for $H > H_c$) or

$$\Theta(H) = \cos^{-1} \left(-\frac{H}{H_c} \right), \quad (6)$$

otherwise. Since the experimental angle is $\theta = \pi/2 - \Theta$ the best fit function is $-\sin^{-1} H/H_c$.

However, our crystals were not mounted on a precise goniometer and we must foresee a misalignment, which has been allowed for in the second order perturbation best fit of the quadrupole-perturbed-NMR peaks vs. applied field (Fig. 2a). The same correction must be applied to the mean field theory, yielding

$$\sin 2\Theta = \frac{H}{H_c} \left(\cos \Theta \sin \alpha \sin^{-1} \frac{H}{H_c} - \sin \Theta \cos \alpha \right). \quad (7)$$

The two curves are show in Fig. S.2, a replica of Fig. 2b, where the colored solid curves are the perfectly aligned $\alpha = 0$ expectations and the grey solid curves are the corresponding expectations for the experimental misalignment. The high field values seem to slowly approach $\frac{\pi}{2}$, clearly outside the simple mean-field predictions.

III. DC MAGNETIZATION

The field dependence of the isothermal magnetization was measured using a commercial Quantum Design superconducting quantum interference device (SQUID) magnetometer, equipped with the vibrating sample magnetometer (VSM) option (SQUID-VSM and MPMS3). Figure S.3 presents the derivative of the isothermal magnetization, measured with the magnetic field along \hat{c} at $T = 2$ K for $\text{Mn}_{1/3}\text{NbS}_2$. The phase transition from the CHM phase is visible in both samples, with $\text{Mn}_{1/3}\text{NbS}_2$ saturating above 5T.

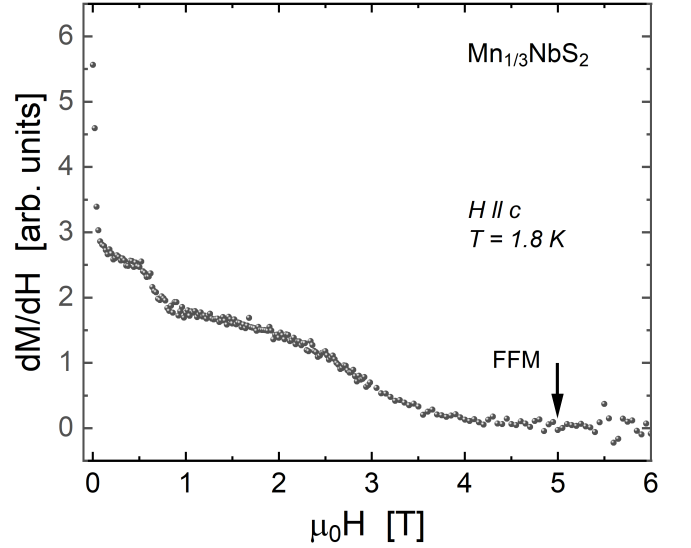


FIG. S.3: Derivative of field dependent isothermal magnetization for $\text{Mn}_{1/3}\text{NbS}_2$ for $\mathbf{H} \parallel \hat{c}$